Ti$_3$C$_2$-MXene Partially Derived Hierarchical 1D/2D TiO$_2$/Ti$_3$C$_2$ Heterostructure Electrode for High-Performance Capacitive Deionization

Ningning Liu, Lanlan Yu, Baojun Liu, Fei Yu, Liqing Li, Yi Xiao, Jinhu Yang, and Jie Ma*

Constructing faradaic electrode with superior desalination performance is important for expanding the applications of capacitive deionization (CDI). Herein, a simple one-step alkalized treatment for in situ synthesis of 1D TiO$_2$ nanowires on the surface of 2D Ti$_3$C$_2$ nanosheets, forming a Ti$_3$C$_2$-MXene partially derived hierarchical 1D/2D TiO$_2$/Ti$_3$C$_2$ heterostructure as the cathode electrode is reported. Cross-linked TiO$_2$ nanowires on the surface help avoid layer stacking while acting as the protective layer against contact of internal Ti$_3$C$_2$ with dissolved oxygen in water. The inner Ti$_3$C$_2$ MXene nanosheets cross over the TiO$_2$ nanowires can provide abundant active adsorption sites and short ion/electron diffusion pathways. . Density functional theory calculations demonstrated that Ti$_3$C$_2$ can consecutively inject electrons into TiO$_2$, indicating the high electrochemical activity of the TiO$_2$/Ti$_3$C$_2$. Benefiting from the 1D/2D hierarchical structure and synergistic effect of TiO$_2$ and Ti$_3$C$_2$, TiO$_2$/Ti$_3$C$_2$ heterostructure presents a favorable hybrid CDI performance, with a superior desalination capacity (75.62 mg g^{-1}), fast salt adsorption rate (1.3 mg g^{-1} min^{-1}), and satisfactory cycling stability, which is better than that of most published MXene-based electrodes. This study provides a feasible partial derivative strategy for construction of a hierarchical 1D/2D heterostructure to overcome the restrictions of 2D MXene nanosheets in CDI.

1. Introduction

Capacitive deionization (CDI) technology, which separates ions by creating electrical double layers (EDLs) or Faradaic processes, has attracted much attention because of its high work efficiency, reduced energy cost, and easy operation.[1] Electrode materials play an essential role in deionization performance. Carbonaceous materials, including activated carbon (AC), carbon nanofibers, and graphene, have broad applications as CDI electrode materials owing to their low cost, large specific surface area (SSA), and superior conductivity.[2] However, carbon materials suffer from relatively inferior desalination capacities (usually <25 mg g^{-1}) and poor electrochemical stabilities owing to the restriction of the EDLs desalination principle, which thwarts their applications in CDI.[3] Alternatively, Faradaic materials, including manganese oxide (MnO$_2$),[4] Prussian blue and its analogs,[5] cobalt oxide (Co$_3$O$_4$),[6] 2D transition metal carbides and nitride (MXene),[7] have been widely studied as CDI electrodes recently

N. Liu, J. Ma
Research Center for Environmental Functional Materials
State Key Laboratory of Pollution Control and Resource Reuse
College of Environmental Science and Engineering
Tongji University
1239 Siping Road, Shanghai 200092, P. R. China
E-mail: jma@tongji.edu.cn

L. Yu, B. Liu
College of Resource and Environmental Engineering
Guizhou University
Guiyang 550025, China

F. Yu
College of Marine Ecology and Environment
Shanghai Ocean University
Shanghai 201306, P. R. China

L. Li, J. Ma
Faculty of Materials Metallurgy and Chemistry
Jiangxi University of Science and Technology
Ganzhou 341000, P. R. China

Y. Xiao
Institute of Materials Science
TU Darmstadt
64287 Darmstadt, Germany

J. Yang
School of Chemical Science and Engineering
Tongji University
1239 Siping Road, Shanghai 200092, P. R. China

ADVANCED
SCIENCE NEWS
www.advancedsciencenews.com

ADVANCED
SCIENCE
Open Access
www.advancedscience.com

because of their pseudocapacitive properties. These Faradaic electrodes capture ions through ion intercalation or reversible redox reactions, which are unconstrained by SSA.[8,9] Among various Faradaic materials, MXene, which is usually expressed by the formula $M_{n+1}X_nT_x$, where M is a transition metal (Ti, Mo, etc.), X is carbon and/or nitrogen, and T_x represents the terminating groups (OH, O, and F), exhibits extraordinary potential for CDI applications owing to its combined performance of a high theoretical capacity, remarkable hydrophilic properties, excellent electrical conductivities, large surface area, and tunable surface functional groups.[10,11] Srimuk et al. first applied $Ti_3C_2T_x$ MXene as an electrode material in a symmetric CDI cell; the average desalination capacity was 13 mg g^{-1} at 1.2 V and sustained the stable performance in 30 CDI cycles.[8]

There are two factors leading to the restrictions on $Ti_3C_2T_x$ MXene desalination performance. First, the restacking of adjacent MXene sheets driven by van der Waals forces reduces the exposure of electrochemical active sites, resulting in a decline in the desalination capacity.[12] The construction of 1D/2D hierarchical nanostructures is an efficient method for solving the above agglomeration issue.[13] 1D nanomaterials prevent 2D MXene nanosheets from restacking and provide abundant active sites. In particular, the 1D channel with a high length-to-diameter ratio will provide rapid charge transfer paths and weak charge transmission resistance during the CDI process.[14] A sandwich-like $Ti_3C_2T_x$ MXene/carbon nanotube (CNT) synthetic self-supporting electrode was synthesized for supercapacitor electrodes by alternately filtrating MXene and CNT dispersions.[13b] It had a distensible interlayer space between the MXene sheets. Nevertheless, the layer-by-layer assembly strategy tends to have a complicated manufacturing operation and induce weak interactions between 1D/2D nanomaterials.[15] The oxidative degradation of MXene is another limitation of its application in CDI. The edges and surface of 2D $Ti_3C_2T_x$ MXene are covered by Ti (II) or Ti (III) suboxide or hydroxide/fluoride. They are prone to be oxidized as Ti (IV) oxide (TiO_2) under ambient air or water,[16] which will result in the loss of primordial superior electrical conductivity and destroy the 2D lamellar structure of MXene, resulting in ungratified electrochemical performance.[17] Numerous studies have been dedicated to mitigating MXene oxidation by limiting its exposure to water and oxygen.[18] Zhao et al. demonstrated that annealing $Ti_3C_2T_x$ MXene films at 600 °C under argon gas partially oxidized the surface of $Ti_3C_2T_x$ MXene and generated TiO_2 cladding on the exterior, which prevented further oxidation of the inner layers.[19] The treated MXene films exhibited almost no changes in chemical composition and structure even after 10 months of storage in water. Surface partially derived MXene with a relatively light oxidation degree can form derivatives such as transition metal oxides (TMO), on the surface while maintaining a part of MXene inside. The formation of a protective TMO layer passivates the edges and surface of MXene, which can preclude the oxidative degradation of the interior structure and enhance the stability of MXene and is beneficial for extending the layer space and improving the capacitance of MXene.[20] Simultaneously, the inherent low electronic conductivity of MXene-derived TMO is effectively alleviated by residual MXene. The comprehensive properties of the hybrids are dramatically enhanced via the cooperative effect of MXene and its derivatives.[21] Previous study has successfully in situ formed TiO_2 nanoparticles on the
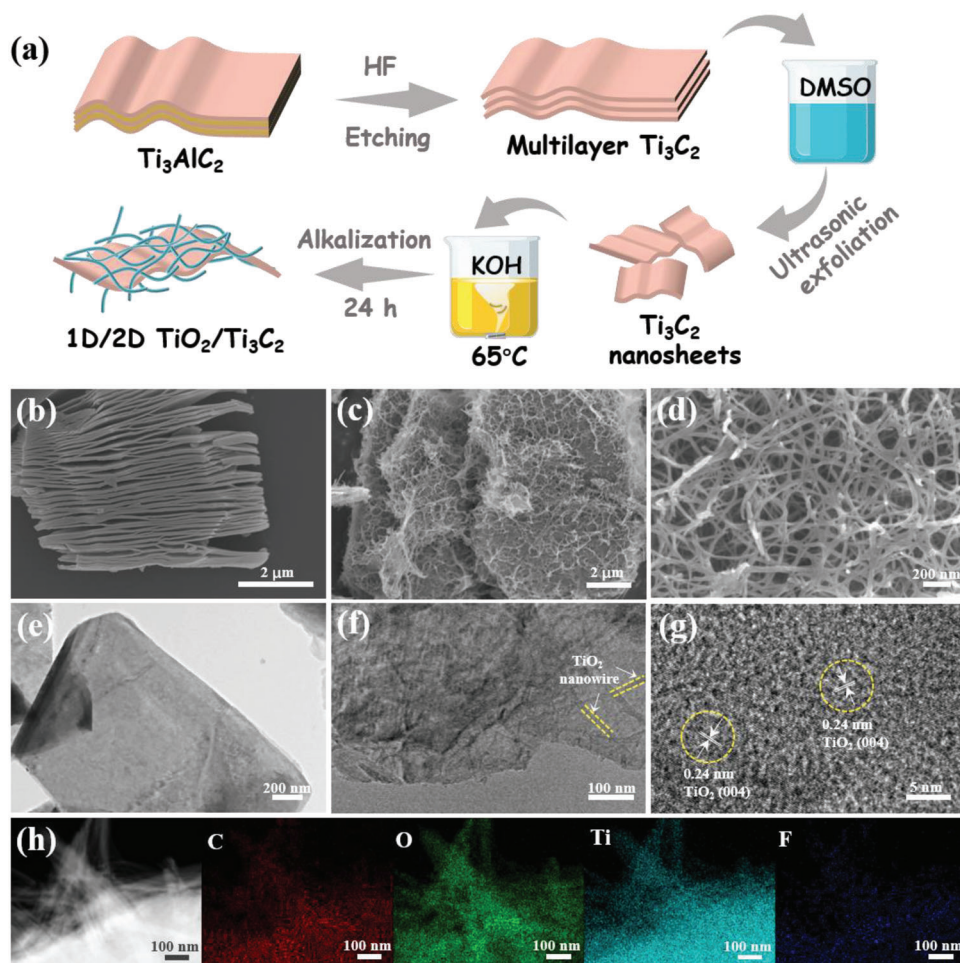
exterior surface of Ti_3C_2 MXene by a hydrothermal method, and the $Ti_3C_2@TiO_2$ hybrid displayed an excellent reversible capacity in lithium ion batteries (302 mA h g^{-1} at 200 mA g^{-1} after 500 cycles).[22] This excellent electrochemical property benefits from the synergy of Ti_3C_2 and TiO_2. However, a significant majority of studies synthesized derived MXene composites through hydrothermal or solvothermal treatment, which required a high temperature or an additional titanium source.[23] It is necessary to develop a facile and manageable method to synthesize partially derived MXene hybrids with well-designed structures for CDI application. As far as we know, there is no report on partially derived MXene materials as CDI electrodes to date.

Herein, a facile one-step alkalized treatment method was applied to partially derivatize Ti_3C_2 MXene in situ to fabricate a hierarchical 1D/2D TiO_2/Ti_3C_2 heterostructure as a cathode material for CDI. Specifically, the cross-linked 1D TiO_2 nanowires grown in situ on the surface of 2D Ti_3C_2 nanosheets can not only further enlarge the spacing of MXene layers and provide abundant ion transport channels for desalination but also work as a protective layer to alleviate the oxidation of inner Ti_3C_2 and thus improve the cycle stability of TiO_2/Ti_3C_2 composites. Moreover, the derived TiO_2 nanowires can supply additional active sites for high Na$^+$ adsorption. The inner Ti_3C_2-preserving 2D framework and outstanding conductivity can facilitate the invertible transmission of electrons and enhance the conductivity of TiO_2. Meanwhile, the 1D channel of TiO_2 nanowires can offer fast charge transport paths. Density functional theory (DFT) calculations demonstrate that the generation of TiO_2-Ti_3C_2 heterostructures accelerates electrons transfer at the interface, which is favorable for promoting electrochemical activity. Profiting from the specific microstructure of 1D/2D hierarchical structure and synergistic effect of TiO_2 and Ti_3C_2, the TiO_2/Ti_3C_2 electrode demonstrates favorable hybrid CDI performance, with a superior desalination capacity of 75.62 mg g^{-1}, satisfactory cycling stability, and low energy consumption, which is better than the majority of published MXene-based electrode materials. And the as-prepared TiO_2/Ti_3C_2 composites also exhibited superior desalination potential in an ultrahigh NaCl concentration of 500×10^{-3} M (173.52 mg g^{-1}) which suggested it is promising for seawater treatment. This work provides an effective method for solving the aggregation and oxidation issues of 2D MXene and exploring surface partially derived MXene-based electrode materials for CDI applications.

2. Results and Discussion

2.1. Material Characterization

The diagram in **Figure 1**a illustrates the production process of the hierarchical 1D/2D TiO_2/Ti_3C_2 heterostructure composite (TiO_2/Ti_3C_2). Multilayer Ti_3C_2 terminated by -OH, -O, and -F surface groups was prepared via hydrofluoric acid (HF) etching of the bulk precursor Ti_3AlC_2 and exhibited a typical accordion sheet-like structure (Figure 1b), suggesting that the Al layer was successfully removed. Ti_3C_2 nanosheets (Figure 1e) were ultimately obtained after dimethyl sulfoxide (DMSO) intercalation and ultrasonic exfoliation. Subsequently, TiO_2/Ti_3C_2 was synthesized through the heat treatment of Ti_3C_2 MXene nanosheets in KOH aqueous solution with vigorous stirring. The surface

ADVANCED
SCIENCE NEWS
www.advancedsciencenews.com

ADVANCED
SCIENCE
Open Access
www.advancedscience.com

Figure 1. a) Schematic diagram for the preparation of TiO_2/Ti_3C_2; SEM images of b) multilayer Ti_3C_2 and c,d) TiO_2/Ti_3C_2; TEM images of e) Ti_3C_2 nanosheets and f) TiO_2/Ti_3C_2; g) HRTEM image of TiO_2/Ti_3C_2; h) dark-filed image of the TiO_2/Ti_3C_2 composite and the corresponding element mapping.

exposed Ti of Ti_3C_2 was first attacked by dissolved oxygen to generate TiO_2 nanoparticles, which acted as nucleation sites. The passive TiO_2 nanoparticles partially dissolved due to the corrosive action of KOH and underwent a dissolution/recrystallization process to form nanowires.

The concentration of KOH was an important parameter affecting the quantity and morphology of the TiO_2 nanowires. Figure S2 in the Supporting Information displays the scanning electron microscope (SEM) images of TiO_2/Ti_3C_2 prepared under 8 M KOH (TiO_2/Ti_3C_2-8). Only a few TiO_2 nanowires heterogenously grew at the surface and edges of Ti_3C_2 MXene with no network of cross-linked structures. As the concentration of KOH solution increased to 10 M, a large number of TiO_2 nanowires ≈10–30 nm in diameter were in situ homogenously grown on the lamellar surface (Figure 1c,d). An increase in KOH concentration is favorable for generating thicker nanowires and cohesive filamentous networks. Vigorous stirring also ensured the uniform formation of slender nanowires, and the formed nanowires were bent because of the difference in force applied to the nanowires during agitation.[24] The transmission electron microscope (TEM) image of TiO_2/Ti_3C_2 (Figure 1f) showed that a certain number

of nanowires were distributed on the flake layer, corresponding to the nanowire/nanosheet composite structure; the Ti_3C_2 nanosheets served as both a support and titanium source during the oxidation process. High-resolution TEM (HRTEM) characterization analysis (Figure 1g) revealed a clear lattice fringe with a lattice spacing of 0.240 nm, representing the (004) crystal plane of anatase TiO_2. Figure 1h presents the dark-field TEM images of TiO_2/Ti_3C_2 and its corresponding elemental mappings. It exhibited a uniform distribution of C, Ti, and O elements, demonstrating that TiO_2 grew uniformly in situ on Ti_3C_2. The atomic ratios of C, O, Ti, and F were 12.90%, 38.68%, 40.84%, and 7.58%, respectively (Table S1, Supporting Information). The heterostructure of TiO_2 and Ti_3C_2 was also demonstrated by the selected area electron diffraction speckles (Figure S3, Supporting Information), which exhibited a set of hexagonal diffraction spots and a concentric diffraction ring with a bright center. The hexagonal diffraction spots represent the Ti_3C_2 phase, while the diffraction ring represents the reflections from polycrystalline anatase TiO_2, indicating the coexistence of Ti_3C_2 and TiO_2.[25]

Figure 2a depicts the X-ray diffraction (XRD) curves of Ti_3C_2 and TiO_2/Ti_3C_2. The characteristic diffraction peaks of (002),
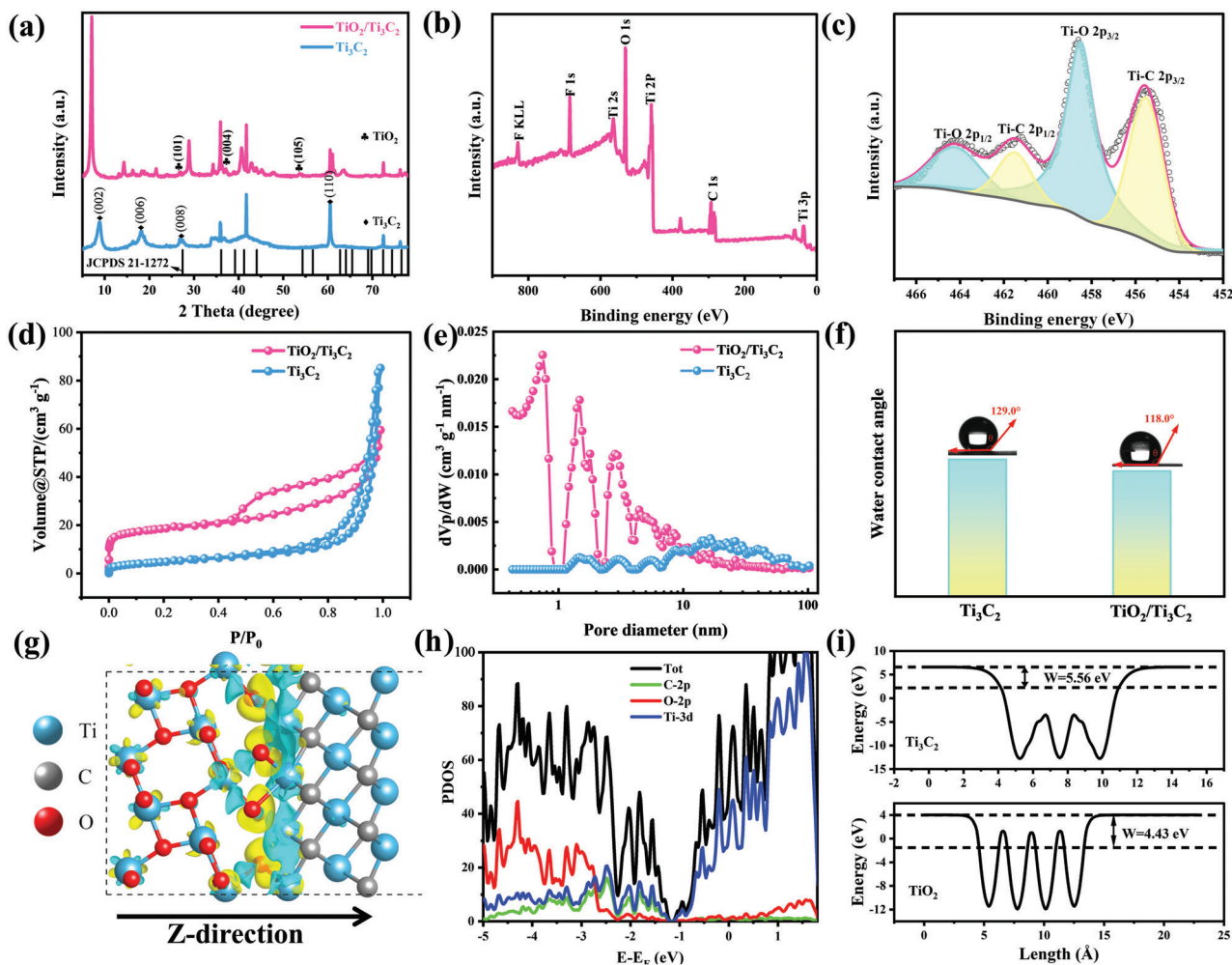
Figure 2. a) XRD pattern of Ti_3C_2 and TiO_2/Ti_3C_2; b) full XPS spectrum of TiO_2/Ti_3C_2; c) XPS spectrum of Ti 2p for TiO_2/Ti_3C_2; d) nitrogen adsorption and desorption isotherm of Ti_3C_2 and TiO_2/Ti_3C_2; e) pore size distribution of Ti_3C_2 and TiO_2/Ti_3C_2; f) water contact angles of Ti_3C_2 and TiO_2/Ti_3C_2; g) charge density difference along the Z direction for TiO_2/Ti_3C_2; h) DOS analysis of TiO_2/Ti_3C_2; i) theoretically calculated work function of Ti_3C_2 and TiO_2.

(006), (008), and (110) were observed in the pattern of Ti_3C_2, which were highly consistent with those reported for Ti_3C_2 MXene.[11] New characteristic peaks were observed at $2\theta = 26.96°$, $37.14°$, and $54.32°$ in the curve of TiO_2/Ti_3C_2, which represented the (101), (004), and (105) planes, respectively, of anatase TiO_2 (JCPDS 21–1271).[26,27] The characteristic (002) peak of Ti_3C_2 shifted from 7.5° to 7.05° for TiO_2/Ti_3C_2, which corresponds to interlayer distances of 11.77 and 12.52 Å, respectively, indicating a further expansion of interlayer spacing.[28] X-ray photoelectron spectroscopy (XPS) spectra were used to explore the surface chemical composition of the composites. The signals of Ti 2p, C 1s, O 1s, and F 1s were found in the survey spectrum of TiO_2/Ti_3C_2 (Figure 2b). Compared with that of the original Ti_3C_2 MXene (Figure S4a, Supporting Information), the atomic content of F substantially decreased, which was due to the substitution of -F groups by -O or -OH groups through the alkali process, and the replacement of F contributed to promoting the specific capacitance.[29] The high-resolution XPS spectrum of Ti 2p for virgin Ti_3C_2 MXene (Figure S4b, Supporting Information) demonstrated that the Ti $2p_{3/2}$ components located at 454.6,

455.5, and 458.7 eV corresponded to Ti-C, Ti-X (a combination of a nanostoichiometric TiC_x ($x < 1$)), and TiO_2, respectively.[30] After alkali treatment, the Ti-X peak at 455.5 eV disappeared, with a decrease in Ti-C peak intensity and an increase in Ti(IV) peak intensity (Figure 2c), indicating that TiO_2 was generated by the partial destruction of Ti_3C_2.[31]

The N_2 adsorption–desorption isotherms of the TiO_2/Ti_3C_2 hybrids displayed a representative type-IV curve with an H3-type hysteresis loop (Figure 2d), indicating the predominant mesoporous structures of the compounds and showing a slit pore geometry due to the stacking of spark particles.[32] The SSA of TiO_2/Ti_3C_2 (50.74 m^2 g^{-1}) was much larger than that of the pristine MXene nanosheets ($S_{BET} = 17.56$ m^2 g^{-1}) due to the growth of TiO_2 nanowires on the interlayer increasing the interlayer space of Ti_3C_2. Figure 2e displays the pore size distributions of Ti_3C_2 and TiO_2/Ti_3C_2, indicating that more mesopores appeared in the TiO_2/Ti_3C_2 structure, which was due to the construction of the 1D/2D hierarchical structure. The larger SSA and abundant mesopores provided more active sites and diffusion paths for ion adsorption and transport during the CDI process.

The above analysis shows that the TiO_2/Ti_3C_2 hybrids with uniform morphology, high purity, and no obvious impurity phase were successfully synthesized. The water contact angle (WCA) measurements were used to explore the wettability of the materials, as shown in Figure 2f. The WCAs of Ti_3C_2 and 1D/2D TiO_2/Ti_3C_2 were 129° and 118°, respectively, indicating that the TiO_2/Ti_3C_2 electrode has better wettability, which is beneficial for ion transport during the desalination process.[27] After alkali treatment, more -OH groups replaced the -F groups on the surface of Ti_3C_2, which strengthened hydrogen bond formation with H_2O. Moreover, the 1D/2D hierarchical structure supplies more exposed spaces for electrolyte permeation.

DFT calculations were applied to discuss the diffusion behaviors at the interface of the heterostructures. The optimized crystal structure of the TiO_2/Ti_3C_2 heterostructure (Figure S5a, Supporting Information) demonstrated the formation of the Ti–O band between the TiO_2 and Ti_3C_2, and the length of the Ti–O band at the interface was 1.98 Å, which is approximately equal to the actual length of the Ti–O band (1.94–2.01 Å) in pristine TiO_2.[33] Interfacial interactions were studied by analyzing the charge density differences. The yellow and cyan areas in Figure 2g refer to electron accumulation and depletion, respectively. Electronic coupling occurred at the interface between the TiO_2 and Ti_3C_2 surfaces, and Ti_3C_2 contributed electrons, while TiO_2 acquired electrons at the Ti_3C_2/TiO_2 heterostructure interface. The planar electrostatic potential of TiO_2/Ti_3C_2 along the Z-direction further demonstrated the electron transport process (Figure S5b, Supporting Information). Figure S5c,d in the Supporting Information presents the densities of states (DOSs) of TiO_2 and Ti_3C_2, respectively. The energy gap of TiO_2 near the Fermi level was ≈1.5 eV, demonstrating the semiconductor properties of TiO_2. The valence bands of Ti_3C_2 across the Fermi level are indicative of its metallic characteristics. Compared to TiO_2 and Ti_3C_2, there were quite a few electronic states across the Fermi level in the TiO_2/Ti_3C_2 heterostructure (Figure 2h), suggesting that the electrical conductivity of TiO_2 was notably improved. The work function describes the electron transfer on the heterojunction interface of TiO_2/Ti_3C_2. The work functions of Ti_3C_2 and TiO_2 (Figure 2i) were 4.43 and 5.56 eV, respectively, implying that Ti_3C_2 tends to continuously inject electrons into TiO_2 to maintain the charge balance, which will significantly improve the electrochemical performance and facilitate the kinetic process of the TiO_2/Ti_3C_2 heterostructure.

2.2. Electrochemical Performance

The cyclic voltammetry (CV) curves of TiO_2/Ti_3C_2 at various scan rates presented an equirectangular shape without observable redox peaks (**Figure 3**a), proving that the composites exhibited Faradaic pseudocapacitive behaviors with a larger capacity. The slight losses in capacity at high scan rates suggested a rapid charge storage principle. TiO_2/Ti_3C_2 also showed excellent cyclic stability, followed by the shapes of the CV curves barely changing after going through 100 cycles, and the specific capacity retention rate was 100.9% (Figure 3b). The capacitance slightly increased after a long cycle, which might be attributed to the contact between the TiO_2 nanowires and Ti_3C_2 nanosheets becoming tighter due to the electroactivation effect during the

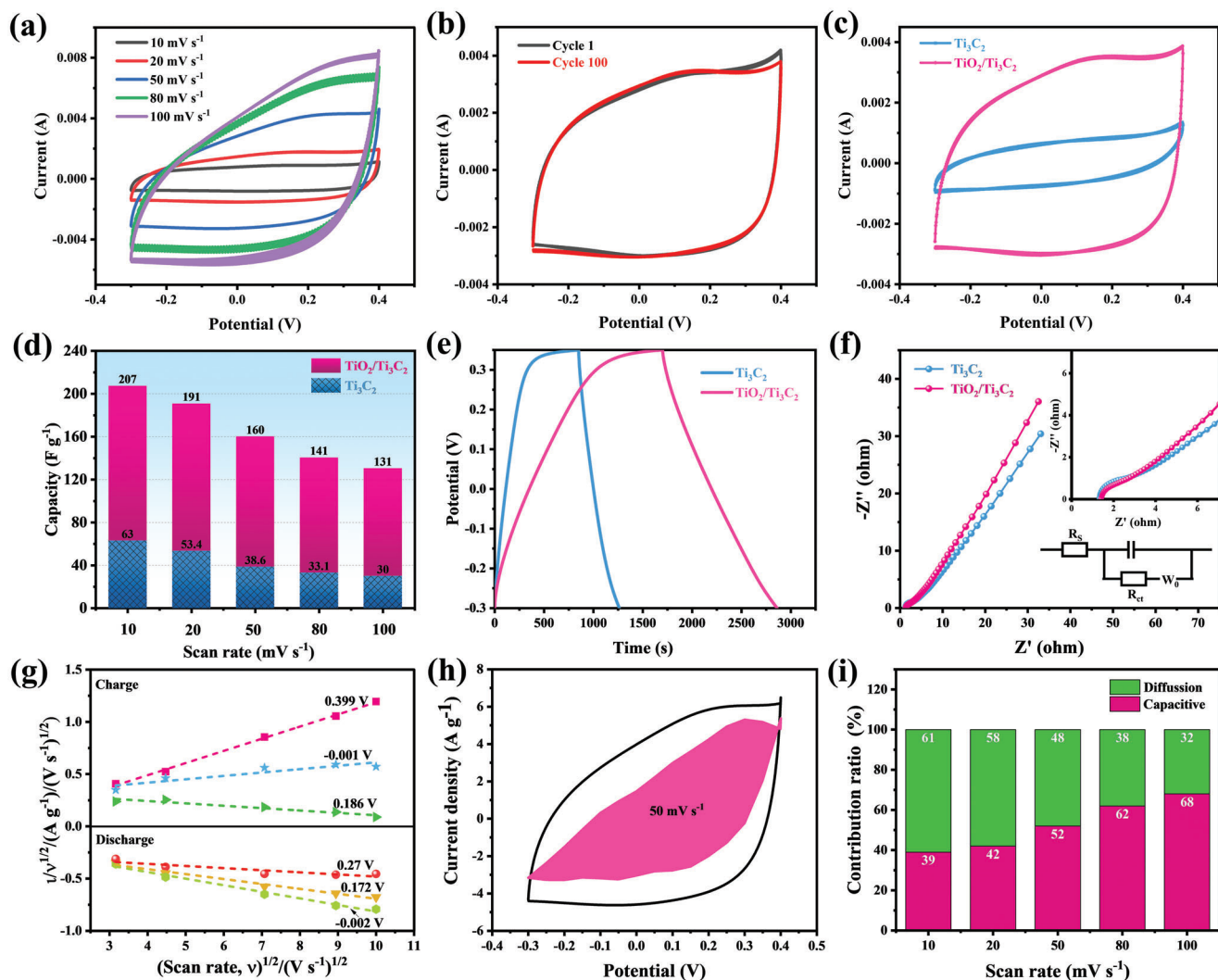ion deintercalation cycle, further improving the electrochemical performance of TiO_2/Ti_3C_2.[34] Figure 3c compares the CV curves of TiO_2/Ti_3C_2 and the initial Ti_3C_2 at 50 mV s^{-1}, and the specific capacitances under different specific currents are displayed in Figure 3d. The specific capacitance of TiO_2/Ti_3C_2 was 207 F g^{-1} at 10 mV s^{-1}, while that of Ti_3C_2 was only 63 F g^{-1}. To thoroughly compare the electrochemical performance of as-prepared TiO_2/Ti_3C_2 with that of previously developed MXene-based electrodes, we measured the electrochemical capacity of the TiO_2/Ti_3C_2 heterostructure in different electrolytes (1 M H_2SO_4, 1 M Li_2SO_4, 1 M Na_2SO_4, and 1 M KOH) using a three-electrode cell configuration (Figure S6a–d, Supporting Information). To estimate the Li$^+$ storage capacity of TiO_2/Ti_3C_2, we also measured its CV profiles in 1 M $LiPF_6$ with a mixture of ethylene carbonate and dimethyl carbonate (1:1 by volume) (Figure S6e, Supporting Information). Table S2 in the Supporting Information lists the capacitance values for the reported state-of-the-art MXene-based heterostructure electrodes in different electrolytes. Remarkably, our work achieved a relatively high specific capacity, which is comparable to or even higher than that of currently developed MXene-based electrodes. The significantly improved specific capacitances were closely related to the increased interlayer spacing and unique 1D/2D nanowire/nanosheet hierarchical structure, which provides more ion adsorption sites.

The galvanostatic charge–discharge (GCD) curves without observable redox peaks exhibited the pseudocapacitive properties of TiO_2/Ti_3C_2 and Ti_3C_2 (Figure 3e), which were consistent with the conclusion of the CV curves. In addition, the charging/discharging process was asymmetric, implying that the ion capture behavior of TiO_2/Ti_3C_2 can be categorized as pseudocapacitive behavior rather than electrical double-layer behavior. The Nyquist plots of TiO_2/Ti_3C_2 and Ti_3C_2 (Figure 3f) fitted by the equivalent circuit model showed a semicircle (Figure 3f inset) and a straight line at low frequency. The charge transfer resistance (R_{ct}) values estimated from the semicircle for Ti_3C_2 and TiO_2/Ti_3C_2 (Table S3, Supporting Information) were 1.25 and 0.81 Ω, respectively. TiO_2/Ti_3C_2 displayed a lower charge transfer resistance, which might be because of the high electrical conductivity of MXene and the abundant ion transmission channels in the TiO_2/Ti_3C_2 hybrid. The electrochemical impedance spectra (EIS) analysis demonstrated that TiO_2/Ti_3C_2 with superior electrical conductivity was conducive to the rapid transport of ions and had an excellent electrochemical performance.[35]

To explore the superior rate performance of the TiO_2/Ti_3C_2 electrode in depth, the proportion of surface-controlled capacitance (capacitor-like contribution) was analyzed (Figure 3g–i).[36] A dominant capacitive contribution was realized for the TiO_2/Ti_3C_2 electrode (52% at 50 mV s^{-1}). The percentage of capacitive contribution increased with increasing scan rate, reaching a maximum of 68% at 100 mV s^{-1} (Figure 3i). Notably, a large capacitance contributes to facilitating fast and reversible ion storage.[37]

2.3. Desalination Performance

A hybrid CDI (HCDI) cell equipped with dual ion-exchange membranes (**Figure 4**a) was used to test the desalination performance of TiO_2/Ti_3C_2 at a specific current. The variations in the

**ADVANCED
SCIENCE NEWS**

www.advancedsciencenews.com

**ADVANCED
SCIENCE**
Open Access

www.advancedscience.com

Figure 3. a) CV curves of TiO_2/Ti_3C_2 at various scan rates; b) CV curves over 100 cycles at a scan rate of 50 mV s^{-1}; c) CV curves of TiO_2/Ti_3C_2 and TiO_2 at a scan rate of 50 mV s^{-1}; d) comparison of capacitance between TiO_2/Ti_3C_2 and Ti_3C_2; e) GCD curves of TiO_2/Ti_3C_2 and Ti_3C_2 at 0.1 A g^{-1}; f) Nyquist plots of TiO_2/Ti_3C_2 and Ti_3C_2; g) plots of $i/v^{1/2}$ versus $v^{1/2}$ at various potentials; h) CV curve at 50 mV s^{-1} where the shaded area represents capacitive contribution; i) capacitive and diffusion contribution ratio at various scan rates.

NaCl concentration, voltage, and current over time under different current densities and cutoff voltages that occurred during the electrosorption/regeneration process are presented in Figure 4b. The NaCl concentration varied linearly with the reaction time and could be restored to its original state, which demonstrated the excellent regeneration performance of the electrode.[38] Moreover, the NaCl concentration decreased during the charging process while increasing during the discharging process, indicating that the adsorption/desorption reactions of Na$^+$/Cl$^-$ occurred during the charging/discharging process. The salt adsorption capacity (SAC) was 75.62 mg g^{-1} at 15 mA g^{-1} and declined to 31.71 mg g^{-1} as the specific current increased to 35 mA g^{-1} (Figure 4c). A large current density contributes to a shorter charging time and large diffusion restriction; thus, abundant active sites are underutilized, resulting in a reduced capacity, while a larger current density can accelerate charge transfer, giving rise to a faster desalination rate. When the current density was 35 mA g^{-1}, the spe-

cific absorption rate (SAR) reached 1.30 mg g^{-1} min^{-1}. When the voltage window increased from −0.8 V/0.8 V to −1.2 V/1.2 V, the average SAC increased from 17.35 to 42.78 mg g^{-1} A larger voltage range with a longer charging time accumulates more charge at the electrode, which is beneficial for the CDI process. Nevertheless, an overly high cutoff voltage is prone to inducing side reactions and reduces the stability of electrodes.[39] The developed TiO_2/Ti_3C_2 electrode in the membrane-free CDI system also exhibited an exceptional desalination capacity (53.3 mg g^{-1} at 15 mA g^{-1}), as shown in Figure S7 in the Supporting Information.

The cycle stability of electrodes is a significant index for judging their CDI properties. The SAC of the TiO_2/Ti_3C_2 electrode remained at a capacity retention ratio of 94% after 60 cycles at a current density of 25 mA g^{-1} (Figure 4e), and even after 200 cycles, the TiO_2/Ti_3C_2 electrode still had a good capacity retention of 71% (Figure S8, Supporting Information), suggesting a
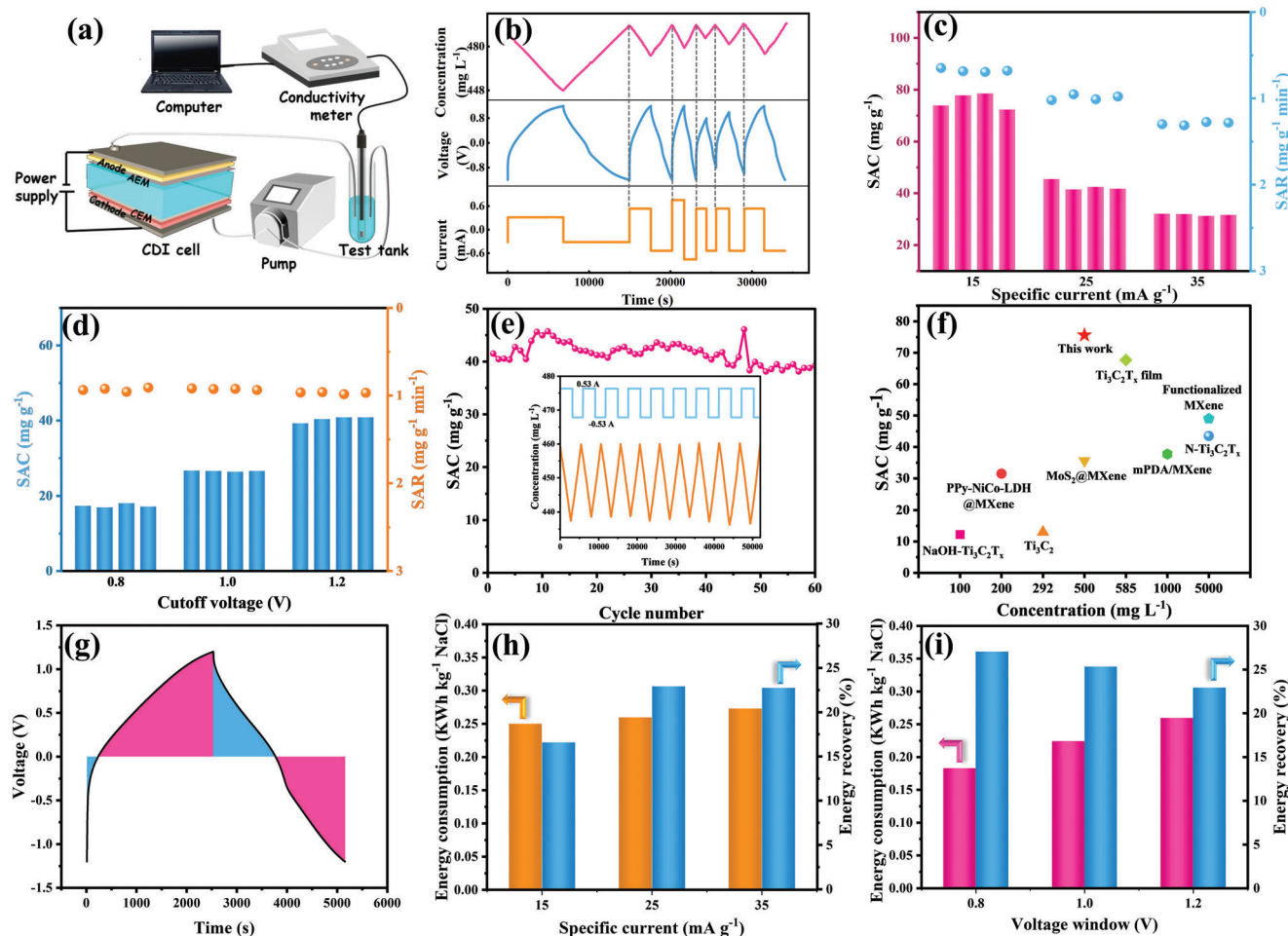
Figure 4. a) Schematic diagram of the CDI system; b) changes in the NaCl concentration, voltage, and current over time under various current densities and voltage windows; salt adsorption capacity and rate of TiO_2/Ti_3C_2 c) under different current densities and d) voltage windows; e) Long-term desalination capacity and the corresponding change in salt concentration over time; f) comparison of the desalination performance of MXene-based composites in NaCl solutions with different concentrations; g) change in voltage over time during the desalination/regeneration process; energy consumption and energy recovery under h) different current densities and i) voltage windows.

preferable desalination cyclicity. The cycle stability under a low current density (15 mA g^{-1}) was also analyzed because the desalination time is longer at lower current densities. The TiO_2/Ti_3C_2 electrode exhibited a good capacity retention ratio of 87% after 40 cycles at 15 mA g^{-1} (Figure S9, Supporting Information), indicating its desalination stability at low current densities. The excellent cycle stability is enhanced by the protection of the wrapped TiO_2 nanowire layer on the surface of the Ti_3C_2 sheet, which delays the oxidation of the inner Ti_3C_2 and improves the stability of the TiO_2/Ti_3C_2 composites.

The CDI properties of various MXene-based electrodes are summarized in Figure 4f and Table S4 in the Supporting Information. To facilitate a comparison with previous reports, the CDI performance was also tested under a constant applied voltage (64.32 mg g^{-1} at 1.2 V over 1 h, Figure S10, Supporting Information). The TiO_2/Ti_3C_2 electrode in this work exhibited an optimum desalination capacity and excellent CDI performance, which was due to the large SSA, abundance of active sites, and short ion diffusion pathway provided by the unique 1D/2D hierarchical structure and good electrochemical performance of the

TiO_2/Ti_3C_2 heterostructure. In addition, the desalination properties of the as-prepared TiO_2/Ti_3C_2 electrode in an ultrahigh NaCl concentration (500 × 10^{-3} M) were analyzed (Figure S11, Supporting Information), and it displayed superior CDI performance (173.52 mg g^{-1} at an operation voltage of 1.2 V for 2 h), suggesting its promising potential for seawater desalination.

Specific energy consumption (SEC) and charge efficiency (CE) are incredibly important for the practical application of CDI. Faradaic materials display less energy consumption per ion adsorption than traditional carbon materials.[40] The total energy consumption during a typical charging/discharging process was obtained from the voltage–time curve (Figure 4g). The blue part represents SEC, and the pink part represents energy recovery. The energy recovery rate (%) was obtained by the ratio of the recovered energy to the consumed energy. First, a self-discharging process occurred under voltages of −1.2 to 0 V; then, the voltage increased from 0 to 1.2 V, causing significant ion intercalation into the electrode materials. When the voltage decreased from 1.2 to 0 V, ions were observably deintercalated from the electrodes and released into the salt solution in the last step.[41]

**ADVANCED
SCIENCE NEWS**

www.advancedsciencenews.com

**ADVANCED
SCIENCE**
Open Access

www.advancedscience.com

Figure 4h,i distinguishes the energy consumption and recovery at different current densities. The SEC was within 0.14–0.41 kWh kg^{-1}-NaCl and 0.13–0.20 kWh kg^{-1}-NaCl at different current densities and various voltage windows, respectively, which was much lower than that of typical carbonaceous materials (i.e., AC with 1.11 kWh kg^{-1}-NaCl). To facilitate a comparison with previous studies, the energy consumption required for treating 1 L feed water (E_V, Wh m^{-3}) is also presented in Figure S12 in the Supporting Information. The E_V was as low as 0.96 Wh m^{-3}, which is much lower than that of typical MXene-based electrodes (Table S4, Supporting Information). The reduction in current density and increase in cutoff voltage result in more energy consumption, and the voltage window exhibits an influence on SEC. A large voltage window easily causes side reactions, such as the reduction of dissolved oxygen, resulting in a lower energy recovery rate. TiO$_2$/Ti$_3$C$_2$ displayed a high CE of 92.81% at a current density of 15 mA g^{-1} (Figure S13, Supporting Information). The relatively high CE is attributed to the low charge transfer resistance of TiO$_2$/Ti$_3$C$_2$, which improves the charge transfer efficiency. Figure S14 in the Supporting Information depicts the ion storage process in the HCDI cell.

The excellent desalination performance of asymmetric AC//TiO$_2$/Ti$_3$C$_2$ is ascribed to the assembly of 1D/2D heterostructures and TiO$_2$/Ti$_3$C$_2$ heterostructures, which display significant SSA, abundant pore structure, and excellent electrochemical properties, leading to a large desalination capacity and fast desalination rate. In addition, the TiO$_2$ coating partially derived from MXene can work as a protective layer to alleviate the oxidation of the remaining Ti$_3$C$_2$, which contributes to maintaining the excellent cycling stability of TiO$_2$/Ti$_3$C$_2$ electrodes.

3. Conclusion

In this study, we prepared a well-designed hierarchical TiO$_2$/Ti$_3$C$_2$ heterostructure by partially derivatizing Ti$_3$C$_2$ MXene in situ. The conductive 2D Ti$_3$C$_2$ nanosheets bridged the 1D TiO$_2$ nanowires to fabricate a 1D/2D hierarchical heterostructure. This unusual morphology not only provides abundant active sites due to the large SSA but also guarantees excellent electrochemical properties under the synergistic effect of TiO$_2$ and Ti$_3$C$_2$. The obtained TiO$_2$/Ti$_3$C$_2$ composite exhibits superior HCDI performance, with a maximum SAC of 75.62 mg g^{-1}, maximum SAR of 1.3 mg g^{-1} min^{-1}, and prominent cyclic stability (without a distinct downtrend after 60 cycles). Remarkably, the desalination performance of TiO$_2$/Ti$_3$C$_2$ is significantly better than that of the majority of published MXene-based materials, revealing the promising application prospects of hierarchical TiO$_2$/Ti$_3$C$_2$ heterostructures in the field of CDI.

4. Experimental Section

Synthesis of Ti$_3$C$_2$ MXene and 1D/2D TiO$_2$/Ti$_3$C$_2$: Ti$_3$AlC$_2$ powders (1.0 g, 400 mesh, 11 Technology Co., Ltd.) were smoothly dispersed into 20 mL of HF (Aladdin Industrial) at 30 °C with constant stirring for 72 h at 300 rpm to etch the Al layer from Ti$_3$AlC$_2$. The sediment was obtained by centrifugation and washed successively with deionized (DI) water and ethanol (Aladdin Industrial) until the suspension pH was higher than 6,

and Ti$_3$C$_2$ was obtained after freeze-drying. The as-prepared Ti$_3$C$_2$ (0.6 g) was mixed with 10 mL of DMSO (Sinopharm Chemical Reagent Co., Ltd.) under stirring for 24 h at room temperature. The synthetic material was cleaned with DI water four times by centrifugation. After that, the mixture underwent ultrasonic treatment for 1 h under argon protection and then the sediment was separated by centrifugation at 3500 rpm for 10 min. The monolayer Ti$_3$C$_2$ was obtained by supernatant freeze-drying. A total of 0.6 g of the monolayer Ti$_3$C$_2$ prepared above was added to a 10 M KOH solution (Sinopharm Chemical Reagent Co., Ltd.) at 65 °C accompanied by stirring for 24 h at 350 rpm. Wash the precipitates with DI water until the pH of supernatant reaches 7. After centrifugation, the samples were freeze-dried to obtain TiO$_2$/Ti$_3$C$_2$ composites. All chemicals and reagents used in this work were used without further purification.

Electrode Preparation: The electrode was prepared as follows: active material (Ti$_3$C$_2$, TiO$_2$/Ti$_3$C$_2$, or active carbon), acetylene black (Sinopharm Chemical Reagent Co., Ltd.), and polyvinylidene fluoride (Shanghai Macklin Biochemical Co., Ltd.) at a weight ratio of 80%:10%:10% were blended in a specified volume of *N*-methyl-2-pyrrolidone (Aladdin Industrial) solvent under stirring for 12 h to obtain a homogenous slurry. Then, the as-prepared slurry was uniformly dropped on graphite paper using a doctor-blade method with a thickness of ≈75 μm. The thin film electrodes were vacuum-dried at 60 °C for 12 h.

Material Characterization: The microstructure of the obtained samples was observed using SEM (Hitachi S-4800/EX-350, Japan), TEM (JEOL-2010F, Japan), and HRTEM (JEM-2010F, Japan). XRD patterns using nickel-filtered Cu Kα radiation ($\lambda = 1.5406$ Å) at 40 kV and 40 mA (Bruker D8 Advance, Germany) were obtained to research the crystalline phase of the samples. XPS was performed using a Kratos Axis Ultra DLD spectrometer (XSAM 800 spectrometer, Kratos Co., UK) with a monochromated Al Kα X-ray source (energy 1486.68 eV) to analyze the surface composition of the materials. The SSA of the samples was measured by a BELSORP instrument (BEL, Japan, Inc.) on the basis of N$_2$ adsorption/desorption isotherms acquired at 77 K by Brunauer–Emmett–Teller (BET) methods. The hydrophilicity of the samples was studied by the WCA test using an optical contact angle measurement system (POWEREACH JC2000, China).

DFT Calculation: The first-principles approach based on DFT was applied to simulate the mutual effect between different components using the Vienna Ab initio Simulation Package (VASP).[42] The Perdew–Burke–Ernzerhof exchange-correlation functional in generalized gradient approximation was used for molecular geometry optimization and total energy computation.[43] To isolate the interactions between each sheet, a 15 Å vacuum was introduced. The cutoff energy of a plane wave base was set as 520 eV to optimize the structure. Brillouin zone integrations were set up with a 3 × 2 × 1 gamma-centered *k*-point for static computations. For all organized geometric optimization structures, the energy convergence accuracy was 1.0×10^{-6} eV, and the force tolerance for geometry optimization was 0.03 eV Å^{-1}. TiO$_2$ (101) and Ti$_3$C$_2$ (001) sections with specific surface carriers were meticulously designed for lattice matching. The lattice constants of the TiO$_2$ (101) model were $u = 7.552$ Å, $v = 10.21$ Å, and $\theta = 90°$. Those of the Ti$_3$C$_2$ (001) model were $u = 7.13$ Å, $v = 10.61$ Å, and $\theta = 90°$. The lattice mismatch was less than 5.5%. The TiO$_2$ (101) model was consisted of 16 Ti atoms and 32 O atoms. During geometric optimization, the bottom half of these atoms was fixed.

Electrochemical and Desalination Experiments: The CV, GCD, and EIS tests were conducted using a CHI 660D electrochemical workstation (Shanghai CH Instruments Co., China) in a 1 M NaCl aqueous solution. The electrochemical tests involved a three-electrode configuration composed of a working electrode, reference electrode (Ag/AgCl electrode), and counter electrode (platinum sheet). Ti$_3$C$_2$ and TiO$_2$/Ti$_3$C$_2$ films (1 × 1 cm^2) were directly used as working electrodes for the electrochemical measurements. The CV curves were obtained between a voltage window of −0.3 to 0.4 V under specific scan rates (10–100 mV s^{-1}). Then, the GCD was measured within the uniform potential window under various current densities (0.1–1 A g^{-1}). The EIS performance was evaluated at a particular frequency range (10^5 to 10^{-2} Hz) with an amplitude of 5 mV.

Batch-mode desalination experiments were performed in NaCl aqueous solution under a continuous circulation system composed of a CDI device, conductivity meter (Mettler Toledo S230, Switzerland), peristaltic

pump (Longer Pump, YZ-1515x), constant current power supply equipment (LAND battery testing system), and NaCl solution tank. The flow-by CDI cell shown in Figure S1 in the Supporting Information was consisted of a cathode (TiO_2/Ti_3C_2) with an area of 4×4 cm^2 and a mass loading of ≈ 16 mg for the active material, an anode (AC), a cation/anion exchange membrane (CEM/AEM), several glass plates and silicone gaskets, and a chamber with a volume of $0.7 \times 5 \times 5$ cm^3. All electrodes were prepared according to the abovementioned method. In the course of operation, 40 mL of NaCl aqueous solution (500 mg L^{-1}) was constantly cycled from the tank to the CDI apparatus and then pumped back into the tank with a flow velocity of 20 mL min^{-1}. A conductivity meter (METTLER TOLEDO S230, Switzerland) was introduced to measure the real-time electrical conductivity. Desalination experiments were performed under a constant current, and the electrodes were subjected to 12 h of electrolyte immersion and five previous charge/discharge CDI cycles. The data obtained in the sixth cycle were used to calculate the desalination capacity (SAC) and the charge efficiency (CE, Λ, %). The effects of different current densities (15, 25, and 35 mA g^{-1}) and cutoff voltages (0.8, 1.0, and 1.2 V) on the SAC of the electrodes were investigated. The SAC was calculated using the total mass of the active materials of the TiO_2/Ti_3C_2 electrode. Specific computational formulas are presented in the Supporting Information.

Supporting Information

Supporting Information is available from the Wiley Online Library or from the author.

Conflict of Interest

The authors declare no conflict of interest.

Data Availability Statement

The data that support the findings of this study are available from the corresponding author upon reasonable request.

[1] a) H. Wang, B. Chen, D.-J. Liu, X. Xu, L. Osmieri, Y. Yamauchi, *Small* **2022**, *18*, 2102477; b) M. Liang, L. Wang, V. Presser, X. Dai, F. Yu, J. Ma, *Adv. Sci.* **2020**, *7*, 2000621; c) J. E. Dykstra, S. Porada, A. van der Wal, P. M. Biesheuvel, *Water Res.* **2018**, *143*, 367; d) M. Elimelech, W. A. Phillip, *Science* **2011**, *333*, 712; e) R. Uwayid, E. N. Guyes, A. N.

Shocron, J. Gilron, M. Elimelech, M. E. Suss, *Water Res.* **2022**, *210*, 117959; f) J. G. Gamaethiralalage, K. Singh, S. Sahin, J. Yoon, M. Elimelech, M. E. Suss, P. Liang, P. M. Biesheuvel, R. L. Zornitta, L. C. P. M. de Smet, *Energy Environ. Sci.* **2021**, *14*, 1095; g) Y. C. Xiong, F. Yu, J. Ma, *Acta. Phys.-Chim. Sin.* **2022**, *38*, 2006037.

[2] a) S. Porada, P. M. Biesheuvel, V. Presser, *Adv. Funct. Mater.* **2015**, *25*, 179; b) P. Ratajczak, M. E. Suss, F. Kaasik, F. Béguin, *Energy Storage Mater.* **2019**, *16*, 126; c) J. Biener, M. Stadermann, M. Suss, M. A. Worsley, M. M. Biener, K. A. Rose, T. F. Baumann, *Energy Environ. Sci.* **2011**, *4*, 656; d) X. Gong, W. Luo, N. Guo, S. Zhang, L. Wang, D. Jia, L. Ai, S. Feng, *J. Mater. Chem. A* **2021**, *9*, 18604; e) K. Singh, G. Li, J. Lee, H. Zuilhof, B. L. Mehdi, R. L. Zornitta, L. C. P. M. D. Smet, *Adv. Funct. Mater.* **2021**, *31*, 2105203; f) A. N. Shocron, E. N. Guyes, H. H. M. Rijnaarts, P. M. Biesheuvel, M. E. Suss, J. E. Dykstra, *Proc. Natl. Acad. Sci. U. S. A.* **2021**, *118*, e2108240118.

[3] a) Q. Li, Y. Zheng, D. Xiao, T. Or, R. Gao, Z. Li, M. Feng, L. Shui, G. Zhou, X. Wang, Z. Chen, *Adv. Sci.* **2020**, *7*, 2002213; b) T. Gao, H. Li, F. Zhou, M. Gao, S. Liang, M. Luo, *Desalination* **2019**, *451*, 133; c) Z. Bo, Z. Huang, C. Xu, Y. Chen, E. Wu, J. Yan, K. Cen, H. Yang, K. Ostrikov, *Energy Storage Mater.* **2022**, *50*, 395; d) F. Yu, P. Y. Yang, Z. Q. Yang, X. C. Zhang, J. Ma, *Chem. Eng. J.* **2021**, *426*, 131900.

[4] a) A. G. El-Deen, N. A. M. Barakat, H. Y. Kim, *Desalination* **2014**, *344*, 289; b) Z. Y. Leong, H. Y. Yang, *ACS Appl. Mater. Interfaces* **2019**, *11*, 13176.

[5] a) W. Shi, X. Liu, T. Deng, S. Huang, M. Ding, X. Miao, C. Zhu, Y. Zhu, W. Liu, F. Wu, C. Gao, S.-W. Yang, H. Y. Yang, J. Shen, X. Cao, *Adv. Mater.* **2020**, *32*, 1907404; b) L. Shi, E. Newcomer, M. Son, V. Pothanamkandathil, C. A. Gorski, A. Galal, B. E. Logan, *Environ. Sci. Technol.* **2021**, *55*, 5412.

[6] H. M. Moustafa, M. M. Nassar, M. A. Abdelkareem, M. S. Mahmoud, M. Obaid, *J. Environ. Chem. Eng.* **2019**, *7*, 103441.

[7] H. Yin, S. Zhao, J. Wan, H. Tang, L. Chang, L. He, H. Zhao, Y. Gao, Z. Tang, *Adv. Mater.* **2013**, *25*, 6270.

[8] P. Srimuk, F. Kaasik, B. Krüner, A. Tolosa, S. Fleischmann, N. Jäckel, M. C. Tekeli, M. Aslan, M. E. Suss, V. Presser, *J. Mater. Chem. A* **2016**, *4*, 18265.

[9] J. Ma, Y. Xiong, X. Dai, F. Yu, *Environ. Sci. Technol. Lett.* **2020**, *7*, 118.

[10] a) J. Nan, X. Guo, J. Xiao, X. Li, W. Chen, W. Wu, H. Liu, Y. Wang, M. Wu, G. Wang, *Small* **2021**, *17*, 1902085; b) S. Zhang, X. Xu, X. Liu, Q. Yang, N. Shang, X. Zhao, X. Zang, C. Wang, Z. Wang, J. G. Shapter, Y. Yamauchi, *Mater. Horiz.* **2022**, *9*, 1708.

[11] M. Naguib, M. Kurtoglu, V. Presser, J. Lu, J. Niu, M. Heon, L. Hultman, Y. Gogotsi, M. W. Barsoum, *Adv. Mater.* **2011**, *23*, 4248.

[12] a) X. Yang, Q. Wang, K. Zhu, K. Ye, G. Wang, D. Cao, J. Yan, *Adv. Funct. Mater.* **2021**, *31*, 2101087; b) J. Sun, W. H. Kong, Z. Y. Jin, Y. Q. Han, L. Y. Ma, X. T. Ding, Y. S. Niu, Y. H. Xu, *Chin. Chem. Lett.* **2020**, *31*, 953; c) X. Y. Liu, Y. Z. Fang, P. C. Liang, J. H. Xu, B. Xing, K. Zhu, Y. Y. Liu, J. J. Zhang, J. Yi, *Chin. Chem. Lett.* **2021**, *32*, 2899.

[13] a) J. Yan, C. E. Ren, K. Maleski, C. B. Hatter, B. Anasori, P. Urbankowski, A. Sarycheva, Y. Gogotsi, *Adv. Funct. Mater.* **2017**, *27*, 1701264; b) M. Q. Zhao, C. E. Ren, Z. Ling, M. R. Lukatskaya, C. Zhang, K. L. Van Aken, M. W. Barsoum, Y. Gogotsi, *Adv. Mater.* **2015**, *27*, 339; c) Z. Lin, D. Sun, Q. Huang, J. Yang, M. W. Barsoum, X. Yan, *J. Mater. Chem. A* **2015**, *3*, 14096.

[14] a) S. D. Ghadge, O. I. Velikokhatnyi, M. K. Datta, P. M. Shanthi, S. Tan, K. Damodaran, P. N. Kumta, *ACS Catal.* **2019**, *9*, 2134; b) Y. Tang, Y. Zhang, J. Deng, D. Qi, W. R. Leow, J. Wei, S. Yin, Z. Dong, R. Yazami, Z. Chen, X. Chen, *Angew. Chem., Int. Ed.* **2014**, *53*, 13488.

[15] R. Zhang, L. Huang, Z. Yu, R. Jiang, Y. Hou, L. Sun, B. Zhang, Y. Huang, B. Ye, Y. Zhang, *Electrochim. Acta* **2019**, *323*, 134845.

[16] a) H.-W. Wang, M. Naguib, K. Page, D. J. Wesolowski, Y. Gogotsi, *Chem. Mater.* **2016**, *28*, 349; b) H. Chen, Y. Wen, Y. Qi, Q. Zhao, L. Qu, C. Li, *Adv. Funct. Mater.* **2020**, *30*, 906996.

[17] a) G. S. Lee, T. Yun, H. Kim, I. H. Kim, J. Choi, S. H. Lee, H. J. Lee, H. S. Hwang, J. G. Kim, D.-W. Kim, H. M. Lee, C. M. Koo, S. O. Kim, *ACS*

Nano **2020**, *14*, 11722; b) J. Zhao, Q. Li, T. Shang, F. Wang, J. Zhang, C. Geng, Z. Wu, Y. Deng, W. Zhang, Y. Tao, Q.-H. Yang, *Nano Energy* **2021**, *86*, 106091.

[18] E. Choi, J. Lee, Y.-J. Kim, H. Kim, M. Kim, J. Hong, Y. C. Kang, C. M. Koo, D. W. Kim, S. J. Kim, *Carbon* **2022**, *191*, 593.

[19] X. Zhao, D. E. Holta, Z. Tan, J.-H. Oh, I. J. Echols, M. Anas, H. Cao, J. L. Lutkenhaus, M. Radovic, M. J. Green, *ACS Appl. Nano Mater.* **2020**, *3*, 10578.

[20] F. Cao, Y. Zhang, H. Wang, K. Khan, A. K. Tareen, W. Qian, H. Zhang, H. Ågren, *Adv. Mater.* **2022**, *34*, 2107554.

[21] S. He, Q. Zhu, R. A. Soomro, B. Xu, *Sustainable Energy Fuels* **2020**, *4*, 4988.

[22] L. Li, G. Jiang, C. An, Z. Xie, Y. Wang, L. Jiao, H. Yuan, *Nanoscale* **2020**, *12*, 10369.

[23] a) L. Chen, X. Ye, S. Chen, L. Ma, Z. Wang, Q. Wang, N. Hua, X. Xiao, S. Cai, X. Liu, *Ceram. Int.* **2020**, *46*, 25895; b) C. Peng, T. Zhou, P. Wei, H. Ai, B. Zhou, H. Pan, W. Xu, J. Jia, K. Zhang, H. Wang, H. Yu, *Chem. Eng. J.* **2022**, *439*, 135685.

[24] Y. Tang, Y. Zhang, J. Deng, J. Wei, H. L. Tam, B. K. Chandran, Z. Dong, Z. Chen, X. Chen, *Adv. Mater.* **2014**, *26*, 6111.

[25] X. Zhang, Y. Liu, S. Dong, Z. Ye, Y. Guo, *Ceram. Int.* **2017**, *43*, 11065.

[26] X. Li, X. Yin, C. Song, M. Han, H. Xu, W. Duan, L. Cheng, L. Zhang, *Adv. Funct. Mater.* **2018**, *28*, 1803938.

[27] S. A. Shah, T. Habib, H. Gao, P. Gao, W. Sun, M. J. Green, M. Radovic, *Chem. Commun.* **2017**, *53*, 400.

[28] a) R. Sun, H.-B. Zhang, J. Liu, X. Xie, R. Yang, Y. Li, S. Hong, Z.-Z. Yu, *Adv. Funct. Mater.* **2017**, *27*, 1702807; b) M.-Q. Zhao, X. Xie, C. E. Ren, T. Makaryan, B. Anasori, G. Wang, Y. Gogotsi, *Adv. Mater.* **2017**, *29*, 1702410.

[29] R. B. Rakhi, B. Ahmed, M. N. Hedhili, D. H. Anjum, H. N. Alshareef, *Chem. Mater.* **2015**, *27*, 5314.

[30] C. Peng, X. Yang, Y. Li, H. Yu, H. Wang, F. Peng, *ACS Appl. Mater. Interfaces* **2016**, *8*, 6051.

[31] U. Alli, K. McCarthy, I.-A. Baragau, N. P. Power, D. J. Morgan, S. Dunn, S. Killian, T. Kennedy, S. Kellici, *Chem. Eng. J.* **2022**, *430*, 132976.

[32] Y. Xiong, F. Yu, S. Arnold, L. Wang, V. Presser, Y. Ren, J. Ma, *Research* **2021**, *2021*, 9754145.

[33] P. Zhang, Y. Li, Y. Zhang, R. Hou, X. Zhang, C. Xue, S. Wang, B. Zhu, N. Li, G. Shao, *Small Methods* **2020**, *4*, 2000214.

[34] a) S. L. Zhang, H. J. Ying, P. F. Huang, J. L. Wang, Z. Zhang, T. T. Yang, W. Q. Han, *ACS Nano* **2020**, *14*, 17665; b) S. L. Zhang, H. J. Ying, B. Yuan, R. Z. Hu, W. Q. Han, *Nano-Micro Lett.* **2020**, *12*, 78.

[35] P. F. Cai, C. J. Su, W. T. Chang, F. C. Chang, C. Y. Peng, I. W. Sun, Y. L. Wei, C. J. Jou, H. P. Wang, *Mar. Pollut. Bull.* **2014**, *85*, 733.

[36] S. Ardizzone, G. Fregonara, S. Trasatti, *Electrochim. Acta* **1990**, *35*, 263.

[37] Y. Liu, X. Gao, K. Wang, X. Dou, H. Zhu, X. Yuan, L. Pan, *J. Mater. Chem. A* **2020**, *8*, 8476.

[38] W. Zhao, M. Ding, L. Guo, H. Y. Yang, *Small* **2019**, *15*, 1805505.

[39] W. Jin, M. Hu, *Sep. Purif. Technol.* **2020**, *237*, 116343.

[40] S. Vafakhah, M. Saeedikhani, S. Huang, D. Yan, Z. Y. Leong, Y. Wang, L. Hou, L. Guo, P. Valdivia y Alvarado, H. Y. Yang, *J. Mater. Chem. A* **2021**, *9*, 10758.

[41] J. Ma, Y. Cheng, L. Wang, X. Dai, F. Yu, *Chem. Eng. J.* **2020**, *384*, 123329.

[42] a) G. Kresse, J. Furthmuller, *Phys. Rev. B* **1996**, *54*, 11169; b) G. Kresse, J. Furthmuller, *Comput. Mater. Sci.* **1996**, *6*, 15; c) G. Kresse, D. Joubert, *Phys. Rev. B* **1999**, *59*, 1758; d) P. E. Blochl, *Phys. Rev. B* **1994**, *50*, 17953.

[43] J. P. Perdew, K. Burke, M. Ernzerhof, *Phys. Rev. Lett.* **1996**, *77*, 3865.

2204041 (10 of 10)